Research Article

Two-photon Absorption and Photoionization of a Bacterial Phytochrome

Thanh Nhut Do [1], David Menendez [2], Dorina Bizhga [2], Emina A. Stojković [2] and John T. M. Kennis [1,*]

*1 - **Department of Physics and Astronomy,** Faculty of Science, Vrije Universiteit Amsterdam, De Boelelaan 1081, 1081 HV Amsterdam, The Netherlands*

*2 - **Department of Biology,** Northeastern Illinois University, 5500 N. St. Louis Ave., Chicago, IL 60625, USA*

***Correspondence to John T.M. Kennis:** j.t.m.kennis@vu.nl (J.T.M. Kennis)*

https://doi.org/10.1016/j.jmb.2023.168357

Edited by Volha Chukhutsina

Abstract

Phytochromes constitute a family of photosensory proteins that are utilized by various organisms to regulate several physiological processes. Phytochromes bind a bilin pigment that switches its isomeric state upon absorption of red or far-red photons, resulting in protein conformational changes that are sensed by the organism. Previously, the ultrafast dynamics in bacterial phytochrome was resolved to atomic resolution by time-resolved serial femtosecond X-ray diffraction (TR-SFX), showing extensive changes in its molecular conformation at 1 picosecond delay time. However, the large excitation fluence of mJ/mm^2 used in TR-SFX questions the validity of the observed dynamics. In this work, we present an excitation-dependent ultrafast transient absorption study to test the response of a related bacterial phytochrome to excitation fluence. We observe excitation power-dependent sub-picosecond dynamics, assigned to the population of high-lying excited state S_n through resonantly enhanced two-photon absorption, followed by rapid internal conversion to the low-lying S_1 state. Inspection of the long-lived spectrum under high fluence shows that in addition to the primary intermediate Lumi-R, spectroscopic signatures of solvated electrons and ionized chromophore radicals are observed. Supported by numerical modelling, we propose that under excitation fluences of tens of μJ/mm^2 and higher, bacterial phytochrome partly undergoes photoionization from the S_n state in competition with internal conversion to the S_1 state in 300 fs. We suggest that the extensive structural changes of related, shorter bacterial phytochrome, lacking the PHY domain, resolved from TR-SFX may have been affected by the ionized species. We propose approaches to minimize the two-photon absorption process by tuning the excitation spectrum away from the S_1 absorption or using phytochromes exhibiting minimized or shifted S_1 absorption.

Introduction

Phytochromes comprise a family of photosensory proteins utilized by bacteria, cyanobacteria, higher plants, and even fungi to regulate the light-induced responses, growth, reproduction and photosynthesis.[1–2] Phytochromes share the photosensory core module comprised of PAS (Per/ARNT/Sim), GAF (cGMP phosphodiesterase/adenylyl cyclase/FhlA) and PHY (phytochrome-specific GAF related) domains. The photosensory core module (PCM) is usually linked to an effector/enzymatic domain. In bacterial phytochromes (BphPs), this is usually a histidine kinase, part of the two-component signaling pathways in bacteria. The PCM covalently binds a bilin chromophore via

a conserved cysteine residue in the PAS domain for BphPs or GAF domain for plant phytochromes (Phys) and cyanobacterial phytochromes (Cphs). The bilin chromophore is an open-chain tetrapyrrole molecule named biliverdin IXα (BV) in BphPs, phytochromobilin (PΦB) in Phys, and phycocyanobilin (PCB) in Cphs. The bilin chromophore acts like a photo-switch to activate the protein function via photo-excitation.

In the dark, most phytochromes adapt the red-absorbing state (Pr state), where the BV A-, B-, and C- rings are stabilized through hydrogen bonding with a pyrrole water molecule located at the center of BV's binding pocket, as well as a carboxylic group of a conserved Asp. The C15═C16 double bond of the BV chromophore adapts a Z configuration in the Pr state (see Figure 1). Upon red light absorption, the bilin chromophore is excited and undergoes Z/E isomerization around the C15═C16 double bond resulting in the 15E pyrrole D-ring clockwise rotation (see Figure 1). The isomerization of bilin subsequently causes the cascaded conformational changes throughout the protein scaffold and eventually forms the far-red-absorbing state (Pfr state) having the absorption spectrum shifted towards longer wavelengths.[2] The Pfr state is structurally distinct from the Pr state by the refolding of PHY 'tongue' from a β-hairpin into an α-helix, which was observed experimentally in the latest cryo-EM structure[3], crystal structures[4–6] as well as solubilized protein.[6–9] The Pr → Pfr photoconversion proceeds via at least two intermediates called Lumi-R, which is formed directly by the bilin photoisomerization at tens to hundreds of picosecond (ps) timescales, and Meta-R, which is formed in tens of microsecond (μs) by thermal relaxation of Lumi-R.[10–11] Several studies have been conducted to determine the detailed mechanism of the Pr → Pfr photoconversion dynamics. Comparing the Fourier transform infrared (FTIR) spectra of cryo-trapped intermediates (Lumi-R and Meta-R), Foerstendorf

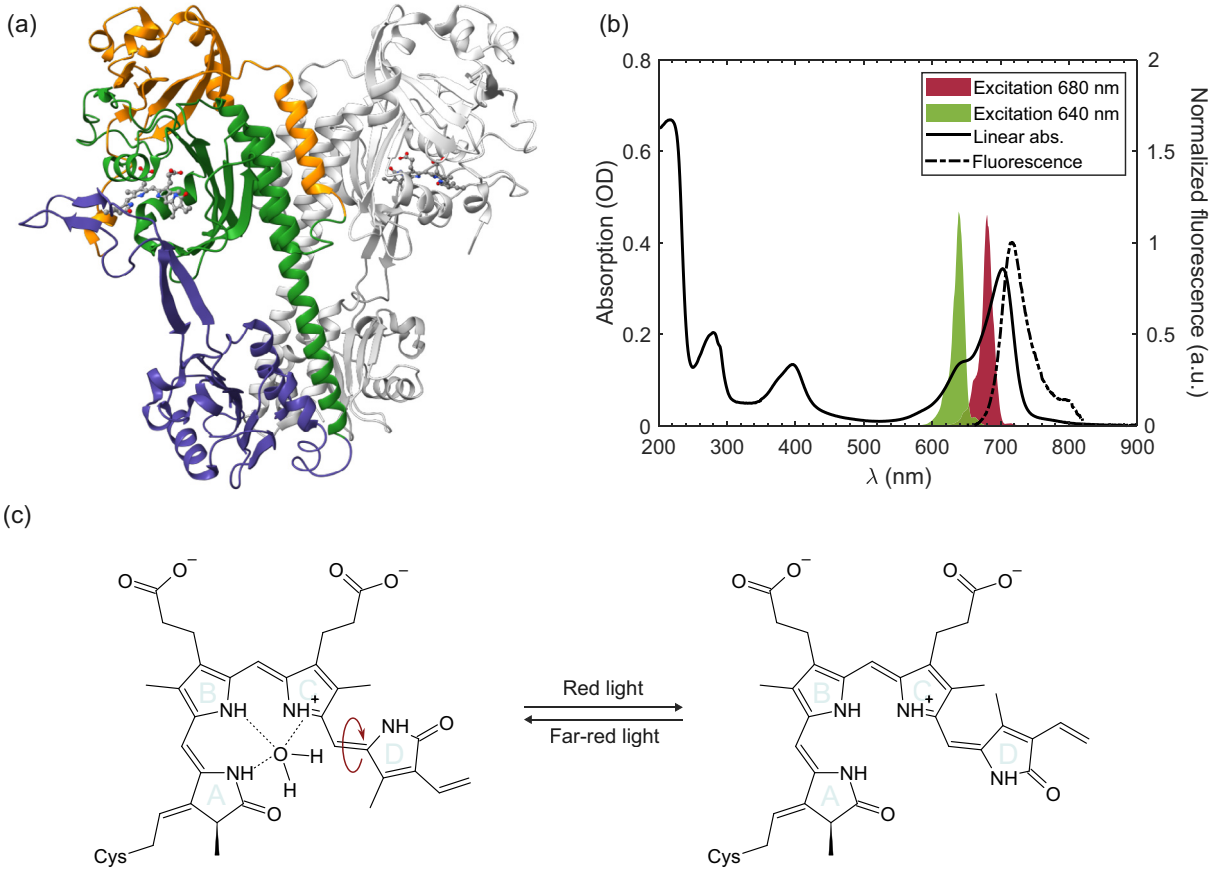

Figure 1. (a) Crystal structure of SaBphP2 at room temperature in Pr form resolved by X-ray diffraction (PDB ID: 6PTQ).[22] The protein is dimeric with one monomeric unit colored in light-grey. The PAS, GAF and PHY domain are colored in orange, green and purple, respectively. The BV chromophore is shown in spheres with C, O and N atoms are colored in grey, red and blue, respectively. (b) Steady-state absorption and fluorescence spectra of SaBphP2 overlaid with the excitation spectra used in the TA measurements. (c) Molecular structures of BV in Pr (left) and Pfr form (right). The curved arrow indicates the isomerization of C15═C16 double-bond upon photoexcitation leading to the clockwise rotation of D-ring.

et al. determined that the pyrrole D-ring is isomerized when Lumi-R is formed.[12] The rotational dynamics of D-ring was directly observed in Cph1 of *Synechocystis* PCC 6803 by Yang *et al.* using polarization resolved visible pump – IR probe spectroscopy. The rotation of D-ring was resolved in the electronic excited state with a time constant of 30 ps.[13] Upon Lumi-R formation, a global restructuring of bilin chromophore may occur, which in turn downshifts several C=C vibrational modes as reported by van Thor *et al.* using transient IR technique.[14] Utilizing femtosecond transient absorption (TA) spectroscopy and comparing different mutations of BphPs from *Rhodopseudomonas palustris*, Toh et al. proposed a detailed molecular mechanism of Lumi-R formation via the twisted D-ring followed by the rupture of hydrogen bonds connecting the D-ring carbonyl with surrounding amino acids.[15–17] This picture was later reaffirmed by Ihalainen et al. using step-scan FTIR combined with molecular dynamics (MD) simulation. The hydrogen bond network around the D-ring was found to be disordered in Lumi-R and lost in the Meta-R state.[9] In addition, using resonant Raman and FTIR spectroscopies, Kraskov et al. further supported the twisted D-ring followed by rupture of hydrogen bonds in BphP2 from *Stigmatella aurantiaca* (SaBphP2) and mutant variant lacking the conserved histidine that forms hydrogen bonds with the D-ring in the Pr state[18]. Interestingly, in the Pfr state of SaBphP2 the protonation of the ring C propionate is observed, which is common among bathy phytochromes but so far has not been reported in prototypical phytochromes.[18] High-level QM/MM-MD calculation was performed on the BphP from *Deinococcus radiodurans* by Salvadori *et al.* and the atomistic detail picture of D-ring rotation via a hula twist was proposed. The hydrogen bond between D-ring carbonyl and a conserved histidine in the GAF domain was broken followed by a rotation of D-ring around C15=C16 double bond and the isomerized product was stabilized by a newly formed hydrogen bond between the N—H proton of D-ring and a nearby tyrosine residue.[19]

Recent developments in X-ray free-electron laser (XFEL) methods provide direct observation of the structural dynamics at atomistic details happening in the protein crystals within several ps after excitation and has been applied to study several biological complexes.[20–29] A time-resolved serial fs X-ray diffraction (TR-SFX) study of the chromophore-binding domain (CBD) consisting of PAS and GAF domains of BphP from *D. radiodurans* ($DrBphP_{CBD}$) provided a near-atomistic picture of the BV chromophore undergoing molecular rearrangement at 1 and 10 ps after excitation.[23] The difference density map revealed a rotation of the D-ring (40–70°) together with extensive structural changes around the binding pocket including the photoejection of the pyrrole water, which subsequently lead to the partial detachment of the BV chromophore from the protein scaffold. All the observed structural changes happened when the BV molecule was still in the electronic excited state (based on the excited-state lifetime of tens to hundreds ps resolved by spectroscopic studies.[17,30] A more recent TR-SFX study of intact PCM from the myxobacterium *Stigmatella aurantiaca* (SaBphP2) was performed with longer delay times of 5 ns and 33 ms to capture the intermediates (likely Lumi-R and Meta-R, respectively).[31] The difference density map of SaBphP2 at 5 ns also revealed the photoejection of pyrrole water, as well as the notable displacement of the whole BV chromophore. However, the TR-SFX study on SaBphP2 observed a clockwise rotation of D-ring[31] instead of the counterclockwise rotation observed in $DrBphP_{CBD}$.[23] Despite the details of structural kinetic information obtained from the TR-SFX experiments, the excitation fluence on the scale of mJ/mm^2 used in such experiment has been a concern since the early days of XFEL development. The weighted average of the observed structural information between undamaged (native) and damaged (*e.g.* ionized) crystals has to be calculated carefully as discussed in a previous study.[32] In bacteriorhodopsin, high femtosecond laser fluences were shown to result in nonlinear photoexcitation of a tryptophan flanking the retinal Schiff base chromophore.[25] A recent TR-SFX study on rhodopsin acknowledged potential multi-photon excitation under their experimental laser fluences,[28] which was required for a sufficiently high occupancy of the structural intermediates.

In this study, we present a series of excitation fluence-dependent TA spectroscopic experiments conducted on the solubilized BphP PAS-GAF-PHY wild-type construct from *S. aurantiaca* (SaBphP2), with a crystal structure at room temperature shown in Figure 1(a). To date, the crystal structure of this wild-type PCM is determined at the highest resolution at cryogenic temperature of any other BphPs.[22] The steady-state absorption spectrum of SaBphP2 in Figure 1 (b) shows characteristic features of the Pr state with a strong absorption band (Q band) that peaks at 700 nm and a vibronic shoulder at 640 nm. These features are consistent with previous studies.[5,22] The fluorescence spectrum mirror images the absorption Q band with a 10-nm Stokes shift. This small Stokes shift corresponds to ~100 cm^{-1} of reorganization energy in the electronic excited state. The main scope of this study is to verify the sensitivity of BphPs to excitation fluences and to determine the photoexcited dynamics of BphPs under a medium-to-high excitation regime.

Results and Discussion

Figure 2(a–c) shows the representative TA spectra of SaBphP2 excited with 680-nm pulses and recorded under three fluences of 2, 5, and 21 nmol photons/cm^2, corresponding to 3.6,

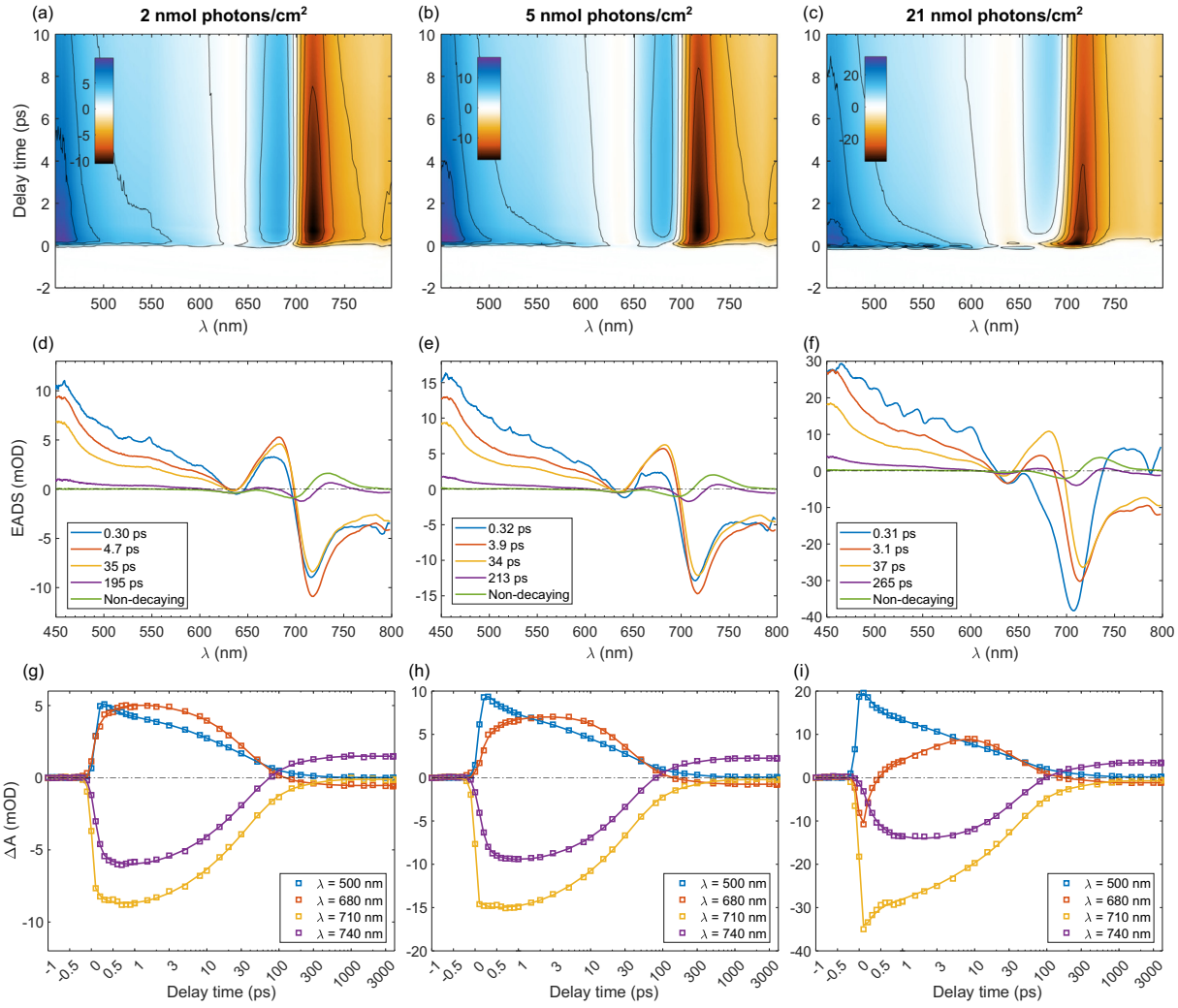

Figure 2. (a–c) Representative TA spectra of SaBphP2 excited at 680 nm with three excitation conditions of 2, 5, and 21 nmol photons/cm^2, corresponding to 3.6, 9.0, and 37 μJ/mm^2 excitation density, respectively. (d–f) Global lifetime analysis results using 5-component sequential kinetic scheme performed using Glotaran software.[33] (g–i) Selected kinetic traces of the data in (a–c) integrated at the indicated wavelength ±2 nm. Squares are the experimental results and curves are the fit obtained from the global lifetime analysis. The delay time axis is linear from −1 to 1 ps and logarithmic afterwards.

9.0, and 37 μJ/mm^2 excitation density, respectively. These, henceforth, will be referred to as low, medium, and high excitation fluence, respectively. The corresponding excitation pulse energies used in the low, medium, and high excitation fluence are 290, 720, and 3000 nJ/pulse yielding the average excitations of 0.46, 1.1, and 4.8 per molecule. Three datasets are qualitatively similar, showing a major negative signal between 700–800 nm originated from the ground-state bleach (GSB) and stimulated emission (SE), a broad positive excited-state absorption (ESA) extending from 600 nm towards the shorter wavelengths, a dip at 630 nm which is likely due to the GSB of the vibronic transition of the Q band, and another ESA signal between 650–700 nm. Despite the similarities, there are noticeable differences when the excitation fluence increases. The ESA feature between 650–700 nm, which appeared almost instantaneously under the low excitation, is delayed and becomes weaker (relative to the major GSB and SE signals) in the high-excitation data. This observation suggests that this ESA is compensated by some additional negative signals appearing at higher excitation.

To gain more insights about the dynamics, we perform the global lifetime analysis (GLA) with a sequential kinetic scheme to extract the main dynamic information. GLA was performed using Glotaran software[33] and the instrument response function (IRF) was modelled by a Gaussian function having full-width at half-maximum (FWHM) of ~120–150 fs. The FWHM of the IRF is effectively

the time-resolution of our experiments. The results from GLA are the evolution-associated difference spectra (EADS) showing the characteristic spectrum decaying with the associated time-constant concomitantly with the rise of the subsequent EADS, *i.e.*, in Figure 1(c), the blue EADS decays with the rate of 1/0.3 ps^{-1} and the orange EADS rises with the same rate. Subsequently, the orange EADS decays at 4.7 ps timescale with the concomitant rise of the yellow EADS and so on. The dynamics of SaBphP2 can be adequately described with a 5-component sequential model as consistent with previous studies.[16–17,34]

The first (~300 fs) and the second (3–5 ps) timescales were previously ascribed as the molecular rearrangement of the BV chromophore in the first excited state (S_1) after fs-excitation.[16] This assignment is due to the almost-constant GSB signal at 720 nm, which does not decay until tens of ps and this major decay is resolved as the third timescale in the GLA (~35 ps). This 35-ps EADS exhibits almost identical spectral features in all of the excitation fluences used in this study as can be seen in Figure 2(d–f). Hence, we assigned this as the *bona fide* isomerization dynamics of the BV chromophore taking place from the S_1 state. In a previous study, comparing this *bona fide* decay between different mutations and between H_2O and D_2O solvents, Toh *et al.* determined that the isomerization begins with a twist of pyrrole D-ring, followed by either hydrogen bond ruptures to form Lumi-R or excited state proton transfer and/or BV mobility to relax back to Pr ground state.[16–17,35] The ~200-ps component is assigned to the minor slower decay pathway and the final EADS having a lifetime of much longer than our experimental temporal window (4 ns) is assigned to be the spectrum of the primary intermediate Lumi-R. The multiple excited-state relaxation pathways observed in GLA is in agreement with other phytochromes systems, including PAS-GAF[17] and PAS-GAF-PHY[16] constructs of BphP from *R. palustris* and *S. auranti-aca*,[34] Cph1 from *Synechocystis*,[36] or single-domain phytochrome All2699g1.[37]

Comparing the 300-fs EADS in Figure 2(d–f), there is a strong excitation dependence, specifically in the 650–700 nm region. Hence, this process cannot be simply described as the molecular rearrangement of the excited BV chromophore. Instead, with increasing excitation fluence, the 300-fs EADS amplitude becomes more negative in the spectral range of 600–700 nm. At the highest excitation fluence, this power-dependent negative signal is strong enough to overwhelm the positive ESA at 650–690 nm and it even affects the subsequent 4-ps EADS. This trend can be observed more clearly by taking the kinetic traces of the data as shown in Figure 2 (g–i). The 680-nm trace of the low fluence is already positive after the initial rise at zero delay time and stays roughly constant until the 35-ps decay takes place, concomitantly with the 710- and 740-nm traces. In contrast, in the high excitation regime, the 680-nm trace is even negative at the early times and gradually turns back to positive before it decays with the 35-ps dynamics.

The 710- and 740-nm kinetic traces in Figure 2(g), which represent GSB and SE signals, respectively, are almost parallel (after the initial rise), indicating that they likely belong to the same excited population under the low fluence. However, at higher fluences, these two kinetic traces start to deviate especially at the sub-ps timescale. In Figure 2(i), the 740-nm trace has a significant increase in amplitude at sub-ps delay times before following the 35-ps dynamics. Together with the fact that the power-dependent negative signal is observed mostly between 600 and 700 nm, coinciding with the ESA feature at 680 nm, which is in turn resonant with the excitation spectrum, we assign the additional signal appearing at the high excitation fluences as due to resonantly enhanced two-photon excitation. Two-photon excitation is resonantly enhanced due to the matching of 680-nm excitation and the ESA, *i.e.*, the absorption of the S_1 state, and sends the BV chromophore into a higher excited state (S_n). At the high-lying state S_n, the chromophore exhibits different spectral signatures, which seems to lack (or minimize) the positive ESA signal at 650–700 nm as compared to the S_1 state. Hence, the more populated S_n state is, the more negative TA can be observed between 650–700 nm, which originates from the negative GSB signal. The S_n population subsequently relaxes back to the S_1 state at a timescale of around 300 fs. This 300-fs $S_n \rightarrow S_1$ internal conversion explains the sub-ps rise of the 740-nm kinetic trace in Figure 2(i), which belongs to the SE signal of the S_1 state, as well as the gradual recovery of the positive ESA of S_1 at 680 nm. Similar resonantly enhanced two-photon absorption processes were previously observed in another photosensory protein – photoactive yellow protein (PYP).[38–40]

To quantify the power dependence of two-photon excited population, we perform a lifetime density analysis (LDA) using custom home-written MATLAB programs. LDA is analogous to the GLA with a parallel kinetic scheme as described in detail elsewhere,[41–42] but instead of decomposing the time-resolved spectroscopic dataset into the finite set of lifetimes and associated spectra, LDA transforms the dataset into a semi-continuous set of lifetimes with the associated spectra indicating the spectral changes. LDA is effectively the numerical inverse Laplace transform of the spectroscopic data.[43] Further details are presented in the Supplementary Information. The resultant two-dimensional plot of wavelength *vs.* lifetime is called the lifetime density map as shown in Figure 3. In this work, LDA is performed with 200 lifetimes, spanning loga-

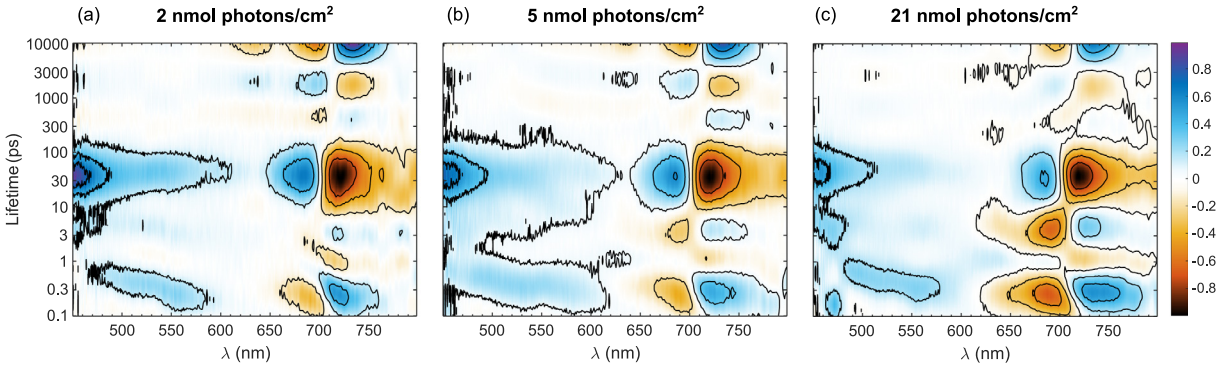

Figure 3. Lifetime density maps obtained from the lifetime density analysis of the three TA datasets presented in Figure 2. The amplitudes of the maps are normalized to the corresponding *bona fide* negative signals at 30–40 ps.

rithmically from 100 fs to 10 ns covering all resolvable dynamics of the experiments. The sign convention of LDA is as follows: the negative signals indicate the 'decrease of negativity', *i.e.*, the decay/rise of negative/positive TA signal, and opposingly, the positive signals represent the 'decrease of positivity' or the rise/decay of negative/-positive TA signal.

Figure 3(a) shows the lifetime density map under the low excitation fluence. The map shows the strongest signal between the lifetimes of 20–100 ps, with the main negative feature at 710–800 nm and two positive features at 650–700 nm and below 600 nm. These are all consistent with the 35-ps EADS in Figure 2(d) showing the *bona fide* decay of the BV excited population in the S_1 state. The feature at the largest lifetime is essentially the non-decaying component, having a positive peak at 710–750 nm and two smaller negative peaks at 630 and 680 nm matching the final EADS in Figure 2(d). Some ringing effects are observed between the lifetimes of 300 ps to 10 ns due to an artefact that occurs when performing LDA on a non-decaying spectral shape. This effect is similar to the sinc function obtained when performing the Fourier transform on a non-decaying function. In the GLA results, beside the major decay at 35-ps lifetime, there is an additional minor decay pathway with a timescale of ~200 ps. This dynamic is located right at the boundary between the major decay feature (20–100 ps) and the ringing effects of the non-decaying signal. Hence, it is not well-resolved in the lifetime density maps.

In the shorter-lifetime region, the features are more subtle, which is not unexpected. According to the GLA results, under low excitation conditions, the TA spectra do not change significantly between 600–750 nm before tens of ps. However, we still can see a small negative-positive pair in Figure 3(a) in the sub-ps timescale representing a sub-ps decay of 670–700 nm signal and a rise of 720–750 nm region. In addition, a decay of ESA signal between 450–600 nm is also observed in the lifetime density map. These observations can be explained as a minor molecular rearrangement of the BV. After the Franck-Condon excitation, the excited chromophore rearranges its nuclear coordinates and relaxes to the equilibrium of the S_1 potential energy surface, yielding a small red-shift of SE (Stokes shift) as well as the changes of ESA. However, if that is the case, this sub-ps feature must remain subtle relative to the *bona fide* 35-ps feature under all excitation conditions. In contrast, when the excitation fluence increases, the sub-ps feature also increases in amplitude and in Figure 3(c), it becomes as significant as the 35-ps decay. Therefore, as discussed above, this sub-ps process must be (partially) contributed by the multi-photon process and we assign this as the resonantly enhanced two-photon excitation from the ground state to the high-lying state S_n via the first-excited state S_1, as discussed in detail above.

In addition, there is another power-dependent feature that can be observed in the several-ps region in the LDMs. This feature matches the 4-ps component obtained from the GLA results. At the lowest fluence, this 4-ps component exhibits almost no spectral changes in 650–750 nm region, and only a very small decay of ESA signal between 450–550 nm. This can be assigned as the molecular rearrangement of the BV chromophore happening in the S_1 state at several ps timescale.[16] However, when the excitation fluence increases, the Q-band region exhibits a significant power-dependent spectral evolution. The lifetime of several ps is too slow for any internal conversion from the high-lying S_n state. Hence, the power dependency of this 4-ps dynamics can be explained by noting that after the sub-ps $S_n \rightarrow S_1$ internal conversion occurs, the BV chromophore relaxes back to the S_1 state but the relaxed molecules drop on different positions of the S_1 potential energy surface. Therefore, an additional spectral evolution happens at 4 ps corresponding to the rearrangement of the BV chromophores having several different configurations (due to the

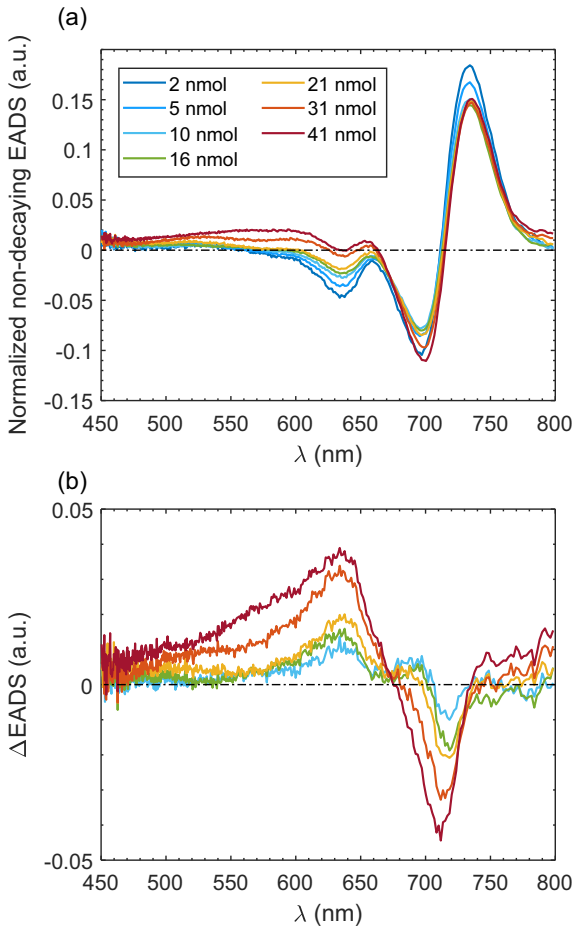

Figure 4. (a) The non-decaying EADS obtained from GLA as shown in Figure 2 for various excitation fluences. These spectra are normalized with the corresponding amplitude of the 35-ps EADS. The unit of fluences is nmol photons/cm^2. (b) The double-difference ΔEADS obtained by subtracting the high-excitation EADS (>10 nmol photons/cm^2) in (a) with the 2-nmol EADS.

$S_n \rightarrow S_1$ relaxation) to reach the final equilibrium before the *bona fide* 35-ps isomerization takes place.

Interestingly, when comparing the long-lived EADS obtained from the GLA, which is usually assigned as the TA spectrum of Lumi-R intermediate, there is also a noticeable power dependence as shown in Figure 4(a). In Figure 4 (a), all non-decaying EADS are normalized to the corresponding amplitude of the *bona fide* 35-ps EADS. This normalization can eliminate the linear dependence of TA signals *vs.* excitation fluence and bring the non-decaying EADS to the same amplitude scale for the ease of spectral features comparison. With the increase of excitation fluence, a broad positive feature between 500–680 nm gradually rises. To visualize the power-dependent trend more clearly, the higher fluence EADS in Figure 4(a) are subtracted with the lowest fluence EADS (2 nmol photons/cm^2) to give the double-difference ΔEADS shown in Figure 4(b). Note that the ΔEADS can only be resolved at sufficient signal-to-noise ratios with the excitation fluences of 10 nmol photons/cm^2 and higher. This is not due to the intrinsic signal-to-noise limitations of the measurements, instead it is due to the fact that the ΔEADS will vanish at low-fluences as the two-photon absorption will not happen to a significant extent and hence, the photoionized species' populations are not high enough to be properly resolved in the ΔEADS.

The ΔEADS in Figure 4(b) are comprised of two components: a broad, positive spectrum overlaid with a negative component, which is highly similar to the steady-state absorption spectrum of SaBphP2. The positive spectrum is almost featureless, extending between 500 and 800 nm and peaks at around 600–650 nm. These properties qualitatively match with the spectrum of solvated electrons as observed in PYP under similar excitation conditions.[39–40,44] Together with the rise of the solvated electron spectrum with the increased excitation density, there is a rise of a negative spectral component strongly resembling the SaBphP2 steady-state absorption spectrum (see Figure 1). There is a clear isosbestic point at 670 nm in Figure 4(b) indicating that the solvated electron spectrum and the negative feature are formed simultaneously. Hence, we assign the negative spectral component as the spectral signature of the ionized BV^{2+} species created together with the solvated electron as a radical pair (in pH 8, the BV chromophore exists as protonated BV^+ form). The appearances of spectral signatures of solvated electron as well as ionized BV^{2+} radical provide evidence that once excited to the S_n state due to resonantly enhanced two-photon excitation, the BV chromophore can undergo photoionization to form the solvated electron – BV^{2+} radical pair. The photoionization and the $S_n \rightarrow S_1$ internal conversion are two competing pathways depopulating the excited population of the S_n state. The photoionized species also indicate that the moderate excitation fluences (the highest value is ~70 μJ/mm^2) used in this study are sufficiently strong to ionize the SaBphP2 to a significant extent.

To quantify the excitation-dependence of two-photon absorption as well as obtain more insights about photoionization dynamics, we analyze in detail two decay dynamics (sub-ps and 35-ps) resolved in the lifetime density maps and compare the results with numerical simulations performed with the kinetic scheme summarized in Figure 5 (a). The system is comprised of three electronic levels denoted as S_0, S_1, and S_n, for the ground, first, and higher excited state, respectively. Three levels are coupled by the transition rates activated within the excitation pulse duration denoted in Figure 5(a) with red arrows. The population of the S_n state is depleted by two competing pathways of

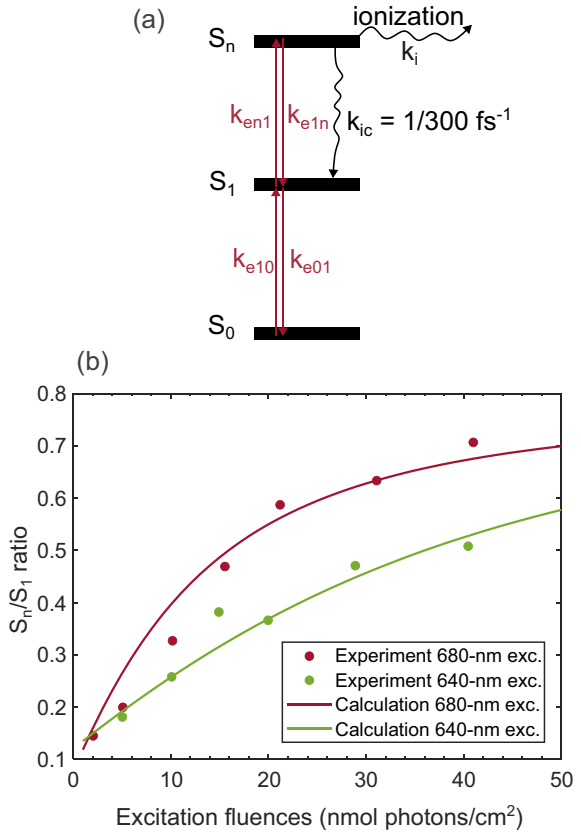

Figure 5. (a) Model kinetic scheme to calculate the degree of photoionization in SaBphP2. (b) Power-dependent ratio of S_n/S_1 population. The dots show the experimental results obtained from the lifetime density maps and the curves show the calculation according to the model in (a) with 680-nm and 640-nm excitation.

ionization and internal conversion [curvy black arrows in Figure 5(a)]. We note that the proposed picture of two competing pathways between photoionization and internal conversion implies that the ionization happens via a quantum tunneling mechanism, *i.e.*, a Marcus-like electron transfer process. If the two-photon excitation would exceed the ionization potential of the BV chromophore, the ionization would happen instantaneously (or more precise, at attosecond timescale)[45] yielding an almost complete depletion of S_1 and S_n populations, which was not observed in our experiments. Secondly, although there is no available literature on the ionization threshold of BV or other linear tetrapyrroles, there are some estimations for cyclic tetrapyrroles giving an ionization potential of around 5–6 eV,[46] which exceeds the energy of two 680-nm photons (~29,000 cm^{-1} or 3.6 eV).

The sub-ps decay of 600–700 nm in the lifetime density map has been interpreted above as the relaxation of S_n population back to S_1 state, creating the rise of SE signal in the 720–800 nm region. We integrate the negative amplitudes of the lifetime density map between 600–700 nm and within 0.1–1 ps lifetime to represent the S_n population relaxation. On the other hand, the integration between 10–100 ps lifetime of negative feature at 710–800 nm represents the population of S_1 state before the isomerization dynamics take place to form Lumi-R. This population includes the directly excited population by the optical pulse as well as the non-ionized portion of S_n that has relaxed. The ratio of these two integrated amplitudes (sub-ps/35-ps) is henceforth called S_n/S_1 ratio and is plotted in Figure 5(b). We note that some approximations were made. Firstly, the 600–700 nm integrated amplitude may also have contributions from an intrinsic red-shift of the SE signal due to the molecular rearrangement of BV.[16] Hence, the power-dependent S_n/S_1 curves are off-set by a small constant and do not trend towards zero at the zero fluence in Figure 5(b). Secondly, as the spectral window for integration is chosen manually, some uncertainties arise due to the differences in transition dipole moments and spectral lineshapes. Hence, the obtained S_n/S_1 ratios need multiplication with a scaling factor, which was determined after an iterative fit (see below) to account for the uncertainties of spectral properties. The scaling step does not affect the power-dependent curvature of the S_n/S_1 curve, hence, our interpretation remains valid.

To extract the rate of ionization (or charge separation rate), we solve the following coupled ordinary differential equations (ODEs)

$$\frac{d[S_0]}{dt} = -k_{e10}[S_0]I(t) + k_{e01}[S_1]I(t) \quad (1)$$

$$\frac{d[S_1]}{dt} = k_{e10}[S_0]I(t) - k_{e01}[S_1]I(t) - k_{en1}[S_1]I(t) + k_{e1n}[S_n]I(t) + k_{ic}[S_n] \quad (2)$$

$$\frac{d[S_n]}{dt} = k_{en1}[S_1]I(t) - k_{e1n}[S_n]I(t) - (k_i + k_{ic})[S_n] \quad (3)$$

$$\frac{d[e]}{dt} = k_i[S_n] \quad (4)$$

The $[S_0]$, $[S_1]$, $[S_n]$ and $[e]$ terms are the population of the ground state, S_1, S_n and the ionized species. Three electronic levels are coupled via the electric field with the transition rates of $k_{e10} = k_{e01} = 4000$ cm^{2}mmol^{-1}ps^{-1} and $k_{en1} = k_{e1n} = 1.5\ k_{e10}$. The transition rate k_{enm} is proportional to the absorption coefficient connecting the population of the m th to the n th electronic level and the numerical values are determined by iteratively solving the ODEs. The ratio between the first and the second transition rates are estimated based on the amplitudes of GSB and ESA signals contributed into the TA spectra (see Supplementary Information). The $S_n \rightarrow S_1$ internal conversion rate k_{ic} is set at (300 fs)$^{-1}$ based on the GLA results. $I(t)$

represents the electromagnetic fields described by a Gaussian function having 150-fs full-width at half-maximum (FWHM). The coupled ODEs are solved with the 4th-order Runge-Kutta integration method[47–48] with 1-fs timesteps integrated from −1 to 5 ps. The *bona fide* 35-ps dynamics of S_1 is neglected in the model as it is very slow compared to the sub-ps dynamics of interest.

The power-dependent S_n/S_1 ratio obtained from the lifetime density maps [data points in Figure 5 (b)] can be compared with the ratio between the calculated non-ionized population of S_n and the calculated S_1 population at 5 ps. The non-ionized portion of S_n population is calculated by subtracting the maximum S_n population during the time frame to the population of ionized species formed at 5 ps (end of the integration time frame). The S_1 population is calculated at 5 ps as the equilibrium population of S_1 before the 35-ps decay happens. This ratio can be directly compared to the experimental data points determined from the lifetime density maps and the calculated curves are overlaid in Figure 5(b). The calculated power-dependent trend is offset with a constant baseline to correct for the amplitude off-set at the zero fluence. This constant off-set can be due to some sub-ps spectral diffusion/molecular rearrangement dynamics of the excited BV chromophore that does not involve the S_n state, yields a small red-shift of SE signal, and stays excitation-independent.[16] The calculated curves are then scaled by multiplying with a factor of 1.2. This scaling factor does not change the curvature of the power-dependent curve. Instead, this acts as a correction factor to adjust for the uncertainty of the chosen integrated spectral range when estimating the experimental S_n/S_1 ratios from the lifetime density maps.

We note that the electric field-coupled transition rates k_{enm} mainly determine the power-dependent curvature of the curves and the small variation of ionization rate k_i does not strongly influence the curvature. Opposingly, the degree of ionization mainly depends on the ratio k_i/k_{ic} and is quite insensitive to the value of the transition rates (k_{eij}). Therefore, we can determine the ionization rate k_i independently from the negative feature of BV^{2+} radical in Figure 4(b). Using the highest fluence data of 41 nmol photons/cm^2, the amplitude of BV^{2+} feature is estimated to be *ca.* −2 mOD. This represents the amount of excited population that has been lost due to ionization. The corresponding GSB signal is obtained as −38 mOD from the spectral decomposition of the *bona fide* 35-ps EADS (see details in Supplementary Information). The degree of ionization can be calculated as 2/38 = 0.053 or 5.3 %. This means that around 5 % of excited BV chromophore is photoionized under the excitation fluence of 41 nmol photons/cm^2 (or 72 μJ/mm^2) with 680-nm excitation.

The ODEs are solved iteratively with ionization rate k_i and the excitation coefficients k_{e10} varied. A good agreement with experimental power-dependent curvature is obtained with the value of $k_{e10} = k_{e01} = 4000$ cm^{2}mmol^{-1}ps^{-1} as mentioned above. The value of k_i = 0.25 ps^{-1} corresponding to the time constant of 4 ps is determined to match the degree of ionization of ∼5 %, which was estimated from the non-decaying EADS as discussed above. As discussed before, in our proposed model, the high-lying state S_n is depopulated via two competing pathways: photoionization and internal conversion back to S_1, with the intrinsic (microscopic) rates k_i and k_{ic}, respectively. Hence, the solvated electron – BV^{2+} radical pair is formed with the rate of $(k_i + k_{ic}) \approx k_{ic}$ (∼1/300 fs^{-1}) and the radical pair is long-lived until several ns or beyond as the spectral signatures of ionized species are resolved in the non-decaying EADS. This observation is consistent with the slow geminate recombination rate of several ns observed in the similar radical pair of PYP.[40]

To reduce the two-photon-induced photoionization processes, one possibility is shifting the excitation wavelength out of the two-photon resonance. This can be performed by investigating the absorption spectrum of the S_1 state. Via spectral decomposition of the *bona fide* 35-ps EADS (details in Supplementary Information), the S_1 absorption spectrum can be estimated with a strong peak at 700 nm with ∼50-nm FWHM. The extinction coefficient of S_1 at 700 nm is estimated to be approx. 110,000 M^{-1} cm^{-1} based on the extinction coefficient of S_0 at 640 nm reported as 27,700 M^{-1} cm^{-1}.[23] The S_1 absorption spectrum extends towards the shorter wavelengths with a

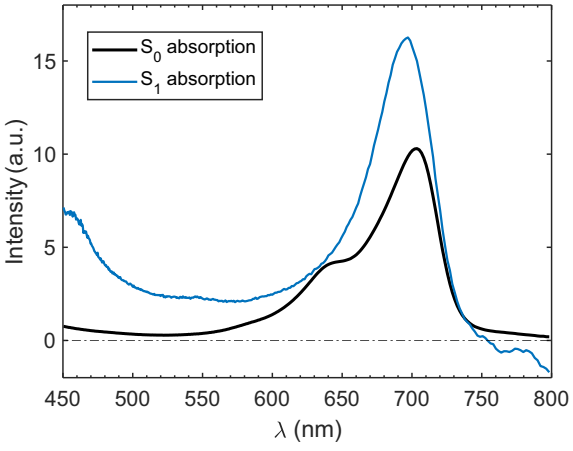

Figure 6. Comparing the absorption spectrum of S_1 obtained from spectral decomposition of 35-ps EADS and the absorption spectrum of the ground state S_0.

minimum at around 550 nm before rising again below 500 nm. Therefore, to minimize the two-photon absorption and ionization processes, the excitation wavelength should be shifted to 550 nm. Unfortunately, there is no ground-state absorption of SaBphP2 in that region (see Figure 6). Hence, a trade-off must be made when shifting the excitation out of 700 nm but still within the absorption window of the complex. In the TR-SFX experiment,[23] the DrBphP$_{CBD}$ was excited with 640 nm. To make a reasonable comparison, we repeat TA measurements with 640-nm excitation and the results are plotted together in Figure 5(b). The calculations are repeated with $k_{e10} = k_{e01} = k_{en1} = k_{e1n} = 2000$ cm^2/mmol (estimate from the absorption at 640 nm relative to 680 nm), the S_n excited manifold is still populated with a significant portion (S_n/S_1 ratio $\sim$ 0.5) and $\sim$3.8 % of excited BV chromophore are photoionized under 40 nmol photons/cm^2 excitation fluence (corresponding to 76 μJ/mm^2). Therefore, it can be concluded that the solubilized BphPs are likely to undergo two-photon induced photoionization when excited at the Q band with the excitation fluences in the scale of tens of μJ/mm^2 or higher.

Applying the calculation with 640-nm excitation and 1 mJ/mm^2 fluence (corresponding to $\sim$700 nmol photons/cm^2), which is a similar excitation condition used in the TR-SFX experiment of DrBphP$_{CBD}$,[23] the degree of ionization is calculated to be 7 %, which follows from the ratio of the rate of ionization k_i versus the $S_n \rightarrow S_1$ internal conversion rate k_{ic}. We note that this 7 % degree of ionization may be underestimated as our model only include two excited electronic levels, while under the regime of mJ/mm^2 excitation, the BV chromophore may undergo multi-photon absorption and access additional ionization pathways.

In the TR-SFX study of DrBphP$_{CBD}$, the excitation fluence was estimated to be decreased by two orders of magnitude due to scattering in the grease medium mixed with crystal solubilization buffer.[23] This would imply that the effective excitation fluence was around 10 μJ/mm^2, which is in the same range of our present study. If this were the case, the present results indicate that even in such a moderate excitation regime, photoionization competes efficiently with Lumi-R formation. Yet, the question remains whether the scattered pump beam photons leave the grease matrix without interacting with the crystals. In essence, the actual excitation fluence in the TR-SFX experiments remains unknown and needs to be characterized more thoroughly to confidently assign the observed transient structural changes to native photoinduced dynamics of bacterial phytochrome.

We note that the observations in TR-SFX on DrBphP$_{CBD}$ are not consistent with spectroscopic evidence. Comparing the steady-state absorption and fluorescence spectra shown in Figure 1(a), the 10-nm Stokes shift between absorption and emission maxima corresponds to around 100 cm^{-1} of reorganization energy. In combination with the mirror symmetry of absorption and fluorescence spectra as can be seen in Figure 1 (b), this observation indicates that the positions of the nuclei in the absorbing and emitting states do not vary appreciably. In contrast, according to the difference density map at 1 ps after excitation, the BV chromophore of DrBphP$_{CBD}$ was observed to undergo a detachment from the binding pocket, with two salt bridges connecting the propionate side chains broken.[23] In addition, the critical pyrrole water that stabilizes BV chromophore was ejected from the CBD pocket. The photoejection of the pyrrole water persists even at the lowest excitation fluence reported in that study (0.2 mJ/mm^2), hence, was considered to be genuinely native. All these extensive structural changes were attributed to the charge redistribution of the excited BV chromophore. However, from an energetic point of view, to eject the pyrrole water from the CBD pocket of DrBphP$_{CBD}$, four hydrogen bonds need to be broken together with two salt bridges. The required energy for breaking all these non-covalent bonds is not consistent with a reorganization energy of the excited state of 100 cm^{-1}. With average energy of a salt bridge in protein that varies between 3 and 5 kcal/mol (1000–1700 cm^{-1})[49] and the weakest hydrogen bond energy is around 10 kJ/mol (836 cm^{-1}),[50] the total free energy required to break two salt bridges and four hydrogen bonds should be at least 5000 cm^{-1}, which differs by more than an order of magnitude as compared to the free energy deduced from the Stokes shift.

The above argument together with our results suggest that the extensive structural changes of the BV chromophore observed in the TR-SFX study may not result from only the native isomerization dynamics. Instead, the observed dynamics may also be related to the ionized BV^{2+} radical formed via resonantly enhanced two-photon excitation, which is observed under tens of μJ/mm^2 fluence in our study. Moreover, at the excitation scale of mJ/mm^2, even higher-order nonlinear processes (like multi-photon excitation) may also contribute to the observed structural changes in the TR-SFX experiment.

Conclusion

In this study, we performed a power-dependent series of transient absorption measurements on the solubilized SaBphP2 with excitation fluence varied on the scale of tens of μJ/mm^2. The TA spectra reveal strong excitation-dependent dynamics, even at moderate excitation powers. On the sub-ps timescale, a strong negative signal appears at medium to high excitation fluences and increases non-linearly relative to the native isomerization dynamics, which was resolved at

~35 ps. The non-linearity of the power dependency is a signature of multi-photon processes. Based on the fact that the power-dependent sub-ps spectral feature coincides with the ESA signal at 680 nm, which was resonant with the excitation pulse, we assign the power-dependent sub-ps dynamics to resonantly enhanced two-photon absorption of the BV chromophore. Under sufficiently high excitation fluences, the BV chromophore can (partially) undergo two-photon absorption to the higher excited state S_n, from where a 300-fs internal conversion takes place and brings the BV chromophore back to the first excited state S_1 before the native isomerization to form photoproduct Lumi-R happens at 35 ps timescale.

Strikingly, by inspecting the long-lived spectra of the photoproduct at various excitation fluences, in addition to the native Lumi-R photoproduct signature, the spectra of solvated electrons together with ionized BV^{2+} radical are observed at high excitation densities and they all persist until several ns timescale. Most likely, such ionization takes place from the transiently populated S_n state in competition with $S_n \rightarrow S_1$ internal conversion. Numerical modelling with a kinetic model involving two competing ionization and $S_n \rightarrow S_1$ internal conversion pathways can extract the ionization rate of 4 ps and about 5 % of excited BV population is ionized under 680-nm and 41 nmol photons/cm^2 (or 72 μJ/mm^2) excitation fluence. The dynamics of SaBphP2 observed in this study are summarized in Figure 7. In conclusion, the excitation fluences of tens of μJ/mm^2 and higher likely result in the formation of non-native ionic BV species in the BphPs. The ionized species may influence the observation of structural changes in TR-SFX experiments. In addition, given that the onset of ionization already occurs at rather moderate excitation densities, care should be taken to avoid such effects in spectroscopic experiments on phytochromes where signal to noise is limited, such as transient (2D) IR and femtosecond stimulated Raman spectroscopy.

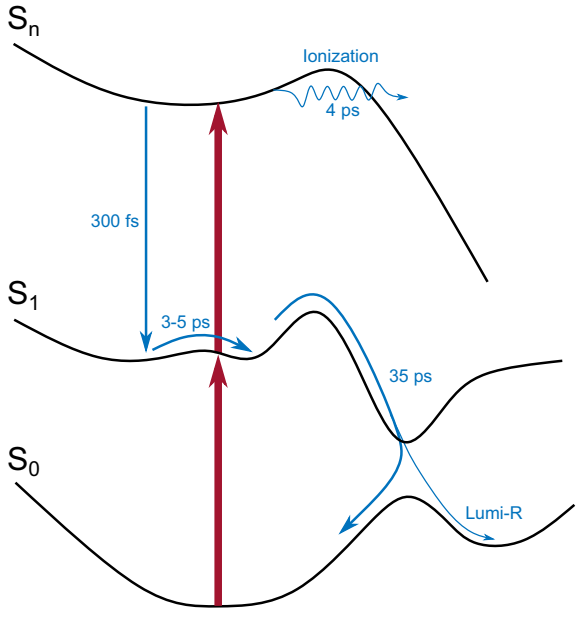

Figure 7. Summary of the dynamics in SaBphP2 observed in this study. The thick red arrows represent the Franck-Condon optical excitations. The blue arrows show the kinetic pathways together with the corresponding time-constants.

The negative impact of two-photon absorption can be minimized by either shifting the excitation wavelength away from the resonant peak of S_1 absorption or *vice versa* (shifting the S_1 absorption spectrum away from the excitation wavelength by using a suitable protein). Both approaches require *a priori* knowledge about the S_1 absorption spectrum of the protein of interest to be considered when choosing the excitation condition for TR-SFX experiments. With a suitable protein having an ESA appropriately tuned away from the excitation pulse, it should be expected that excitation fluences of mJ/mm^2 may be employed with a lower probability of ionizing the chromophore. In that regard, it is interesting to note that ESA maxima and intensity can vary considerably among phytochromes: in RpBphP3, the ESA appears to be red-shifted with respect to the ground-state absorption band, peaking at 740 nm,[16–17] while in engineered fluorescent phytochrome iRFP702, which derives from RpBphP6, it peaks at 730 nm.[35]

Materials and Methods

The SaBphP2 PAS-GAF-PHY wild-type construct was prepared as described previously.[51] The proteins were kept frozen at −80 °C and thawed before using. Sample was diluted with 20 mM Tris.HCl, 50 mM NaCl, pH 8 buffer until the optical density of the Q band maximum reached 0.2 mm^{-1}.

Femtosecond transient absorption (TA) spectroscopy setup was described elsewhere in details.[52] In brief, the 1-kHz, 800-nm output from a Ti:sapphire regenerative amplifier (Libra, Coherent) was used to pump an optical parametric amplifier (OPerA Solo) to generate the excitation pulses centering at the desired wavelengths. A small fraction of 800-nm beam was focused on a 4-mm YAG crystal to generate a supercontinuum spanning 450–850 nm and was used as the probe pulse. The pump pulse is focused by a UV-fused silica lens before attenuated by a neutral density filter to obtain the desired excitation fluence at the sample position with the spot size of ~300 μm (1/e^2 diameter). The probe beam was focused by a concave mirror to the spot size of 60–80 μm at the overlap. The polarization of the pump is set to be 'magic angle' 54.7° with respect to the probe's to eliminate the reorientation

dynamics. Delay time was scanned linearly between −3.5 to 1 ps for dispersion correction and logarithmically thereafter until 3.8 ns. The probe beam was then spectrally dispersed on a CCD array using a prism spectrometer (Entwicklungsbüro Stresing).

The sample was circulated through a 2-mm quartz cuvette by a peristatic pump with the flow rate of *ca.* 50 mL/min. The sample reservoir was kept under constant illumination of 780-nm LED (Thorlabs M780L3) to convert all Pfr photoproduct back to the Pr form.

CRediT authorship contribution statement

Thanh Nhut Do: Methodology, Software, Validation, Formal analysis, Investigation, Data curation, Writing – original draft, Writing – review & editing, Visualization. **David Menendez:** Investigation. **Dorina Bizhga:** Investigation. **Emina A. Stojković:** Conceptualization, Methodology, Resources, Writing – review & editing, Supervision, Project administration, Funding acquisition. **John T.M. Kennis:** Conceptualization, Methodology, Validation, Resources, Writing – review & editing, Supervision, Project administration, Funding acquisition.

DECLARATION OF COMPETING INTEREST

The authors declare that they have no known competing financial interests or personal relationships that could have appeared to influence the work reported in this paper.

Acknowledgement

E.A.S. was supported by NSF-MCB-EAGER grant 1839513 and NSF STC BioXFEL center award 6227. T.N.D. was supported by the Netherlands Organization for Scientific Research (NWO) through the Nanoregulators of Photosynthesis consortium grant to J.T.M.K. This work was supported by a NWO Middelgroot investment grant to J.T.M.K.

Appendix A. Supplementary material

Supplementary material to this article can be found online at https://doi.org/10.1016/j.jmb.2023.168357.

Received 28 July 2023;
Accepted 2 November 2023;
Available online 7 November 2023

Keywords:
phytochrome;
biliverdin;
transient absorption spectroscopy;
power titration;
solvated electron

References

1. Rockwell, N.C., Lagarias, J.C., (2010). A brief history of phytochromes. *ChemPhysChem* **11**, 1172–1180.
2. Rockwell, N.C., Su, Y.-S., Lagarias, J.C., (2006). Phytochrome structure and signaling mechanisms. *Annu. Rev. Plant Biol.* **57**, 837–858.
3. Wahlgren, W.Y., Claesson, E., Tuure, I., Trillo-Muyo, S., Bódizs, S., Ihalainen, J.A., Takala, H., Westenhoff, S., (2022). Structural mechanism of signal transduction in a phytochrome histidine kinase. *Nature Commun.* **13**, 7673.
4. Burgie, E.S., Wang, T., Bussell, A.N., Walker, J.M., Li, H., Vierstra, R.D., (2014). Crystallographic and electron microscopic analyses of a bacterial phytochrome reveal local and global rearrangements during photoconversion. *J. Biol. Chem.* **289**, 24573–24587.
5. Burgie, E.S., Zhang, J., Vierstra, R.D., (2016). Crystal structure of deinococcus phytochrome in the photoactivated state reveals a cascade of structural rearrangements during photoconversion. *Structure* **24**, 448–457.
6. Takala, H., Björling, A., Berntsson, O., Lehtivuori, H., Niebling, S., Hoernke, M., Kosheleva, I., Henning, R., et al., (2014). Signal amplification and transduction in phytochrome photosensors. *Nature* **509**, 245–248.
7. Buhrke, D., Michael, N., Hamm, P., (2022). Vibrational couplings between protein and cofactor in bacterial phytochrome Agp1 revealed by 2D-IR spectroscopy. *Proc. Natl. Acad. Sci.* **119**, e2206400119
8. Stojković, E.A., Toh, K.C., Alexandre, M.T.A., Baclayon, M., Moffat, K., Kennis, J.T.M., (2014). FTIR spectroscopy revealing light-dependent refolding of the conserved tongue region of bacteriophytochrome. *J. Phys. Chem. Letters* **5**, 2512–2515.
9. Ihalainen, J.A., Gustavsson, E., Schroeder, L., Donnini, S., Lehtivuori, H., Isaksson, L., Thöing, C., Modi, V., et al., (2018). Chromophore-protein interplay during the phytochrome photocycle revealed by step-scan FTIR spectroscopy. *J. Am. Chem. Soc.* **140**, 12396–12404.
10. Kübel, J., Chenchiliyan, M., Ooi, S.A., Gustavsson, E., Isaksson, L., Kuznetsova, V., Ihalainen, J.A., Westenhoff, S., et al., (2020). Transient IR spectroscopy identifies key interactions and unravels new intermediates in the photocycle of a bacterial phytochrome. *PCCP* **22**, 9195–9203.
11. Borucki, B., von Stetten, D., Seibeck, S., Lamparter, T., Michael, N., Mroginski, M.A., Otto, H., Murgida, D.H., et al., (2005). Light-induced proton release of phytochrome is coupled to the transient deprotonation of the tetrapyrrole chromophore. *J. Biol. Chem.* **280**, 34358–34364.
12. Foerstendorf, H., Benda, C., Gärtner, W., Storf, M., Scheer, H., Siebert, F., (2001). FTIR studies of phytochrome photoreactions reveal the CO bands of the chromophore: Consequences for its protonation states,

conformation, and protein interaction. *Biochemistry* **40**, 14952–14959.
13. Yang, Y., Linke, M., von Haimberger, T., Hahn, J., Matute, R., González, L., Schmieder, P., Heyne, K., (2012). Real-time tracking of phytochrome's orientational changes during Pr photoisomerization. *J. Am. Chem. Soc.* **134**, 1408–1411.
14. van Thor, J.J., Ronayne, K.L., Towrie, M., (2006). Formation of the early photoproduct lumi-R of cyanobacterial phytochrome Cph1 observed by ultrafast mid-infrared spectroscopy. *J. Am. Chem. Soc.* **129**, 126–132.
15. Toh, K.C., Stojković, E.A., Rupenyan, A.B., van Stokkum, I. H.M., Salumbides, M., Groot, M.-L., Moffat, K., Kennis, J.T. M., (2010). Primary reactions of bacteriophytochrome observed with ultrafast mid-infrared spectroscopy. *Chem. A Eur. J.* **115**, 3778–3786.
16. Toh, K.C., Stojković, E.A., van Stokkum, I.H.M., Moffat, K., Kennis, J.T.M., (2010). Proton-transfer and hydrogen-bond interactions determine fluorescence quantum yield and photochemical efficiency of bacteriophytochrome. *Proc. Natl. Acad. Sci.* **107**, 9170–9175.
17. Toh, K.C., Stojković, E.A., van Stokkum, I.H.M., Moffat, K., Kennis, J.T.M., (2011). Fluorescence quantum yield and photochemistry of bacteriophytochrome constructs. *PCCP* **13**, 11985–11997.
18. Kraskov, A., Buhrke, D., Scheerer, P., Shaef, I., Sanchez, J.C., Carrillo, M., Noda, M., Feliz, D., et al., (2021). On the role of the conserved histidine at the chromophore isomerization site in phytochromes. *J. Phys. Chem. B* **125**, 13696–13709.
19. Salvadori, G., Macaluso, V., Pellicci, G., Cupellini, L., Granucci, G., Mennucci, B., (2022). Protein control of photochemistry and transient intermediates in phytochromes. *Nature Commun.* **13**, 6838.
20. Chreifi, G., Baxter, E.L., Doukov, T., Cohen, A.E., McPhillips, S.E., Song, J., Meharenna, Y.T., Soltis, S.M., et al., (2016). Crystal structure of the pristine peroxidase ferryl center and its relevance to proton-coupled electron transfer. *Proc. Natl. Acad. Sci.* **113**, 1226–1231.
21. Suga, M., Akita, F., Sugahara, M., Kubo, M., Nakajima, Y., Nakane, T., Yamashita, K., Umena, Y., et al., (2017). Light-induced structural changes and the site of O=O bond formation in PSII caught by XFEL. *Nature* **543**, 131–135.
22. Sanchez, J.C., Carrillo, M., Pandey, S., Noda, M., Aldama, L., Feliz, D., Claesson, E., Wahlgren, W.Y., et al., (2019). High-resolution crystal structures of a myxobacterial phytochrome at cryo and room temperatures. *Struct. Dyn.* **6**, 054701
23. Claesson, E., Wahlgren, W.Y., Takala, H., Pandey, S., Castillon, L., Kuznetsova, V., Henry, L., Panman, M., et al., (2020). The primary structural photoresponse of phytochrome proteins captured by a femtosecond X-ray laser. *eLife* **9**, e53514.
24. Nogly, P., Weinert, T., James, D., Carbajo, S., Ozerov, D., Furrer, A., Gashi, D., Borin, V., et al., (2018). Retinal isomerization in bacteriorhodopsin captured by a femtosecond x-ray laser. *Science* **361**, eaat0094.
25. Nass, K.G., Colletier, J.-P., Grünbein, M.L., Yang, Y., Stensitzki, T., Batyuk, A., Carbajo, S., Doak, R.B., et al., (2019). Three-dimensional view of ultrafast dynamics in photoexcited bacteriorhodopsin. *Nature Commun.* **10**, 3177.
26. Skopintsev, P., Ehrenberg, D., Weinert, T., James, D., Kar, R.K., Johnson, P.J.M., Ozerov, D., Furrer, A., et al., (2020). Femtosecond-to-millisecond structural changes in a light-driven sodium pump. *Nature* **583**, 314–318.
27. Yun, J.-H., Li, X., Yue, J., Park, J.-H., Jin, Z., Li, C., Hu, H., Shi, Y., et al., (2021). Early-stage dynamics of chloride ion–pumping rhodopsin revealed by a femtosecond X-ray laser. *Proc. Natl. Acad. Sci.* **118**, e2020486118
28. Gruhl, T., Weinert, T., Rodrigues, M.J., Milne, C.J., Ortolani, G., Nass, K., Nango, E., Sen, S., et al., (2023). Ultrafast structural changes direct the first molecular events of vision. *Nature* **615**, 939–944.
29. Oda, K., Nomura, T., Nakane, T., Yamashita, K., Inoue, K., Ito, S., Vierock, J., Hirata, K., et al., (2021). Time-resolved serial femtosecond crystallography reveals early structural changes in channelrhodopsin. *eLife* **10**
30. Lehtivuori, H., Rissanen, I., Takala, H., Bamford, J., Tkachenko, N.V., Ihalainen, J.A., (2013). Fluorescence properties of the chromophore-binding domain of bacteriophytochrome from deinococcus radiodurans. *J. Phys. Chem. B* **117**, 11049–11057.
31. Carrillo, M., Pandey, S., Sanchez, J., Noda, M., Poudyal, I., Aldama, L., Malla, T.N., Claesson, E., et al., (2021). High-resolution crystal structures of transient intermediates in the phytochrome photocycle. *Structure* **29**, 743–754.e744.
32. Lomb, L., Barends, T.R.M., Kassemeyer, S., Aquila, A., Epp, S.W., Erk, B., Foucar, L., Hartmann, R., et al., (2011). Radiation damage in protein serial femtosecond crystallography using an x-ray free-electron laser. *Phys. Rev. B* **84**, 214111
33. Snellenburg, J.J., Laptenok, S.P., Seger, R., Mullen, K.M., Stokkum, I.H.M., (2012). Glotaran: A Java-based graphical user interface for the R package TIMP. *J. Stat. Softw.* **49**
34. Mathes, T., Ravensbergen, J., Kloz, M., Gleichmann, T., Gallagher, K.D., Woitowich, N.C., St. Peter, R., Kovaleva, S.E., et al., (2014). Femto- to microsecond photodynamics of an unusual bacteriophytochrome. *J. Phys. Chem. Letters* **6**, 239–243.
35. Zhu, J., Shcherbakova, D.M., Hontani, Y., Verkhusha, V. V., Kennis, J.T.M., (2015). Ultrafast excited-state dynamics and fluorescence deactivation of near-infrared fluorescent proteins engineered from bacteriophytochromes. *Sci. Rep.* **5**, 12840.
36. Kim, P.W., Rockwell, N.C., Martin, S.S., Lagarias, J.C., Larsen, D.S., (2014). Dynamic inhomogeneity in the photodynamics of cyanobacterial phytochrome Cph1. *Biochemistry* **53**, 2818–2826.
37. Slavov, C., Fischer, T., Barnoy, A., Shin, H., Rao, A.G., Wiebeler, C., Zeng, X., Sun, Y., et al., (2020). The interplay between chromophore and protein determines the extended excited state dynamics in a single-domain phytochrome. *Proc. Natl. Acad. Sci.* **117**, 16356–16362.
38. Changenet-Barret, P., Plaza, P., Martin, M.M., (2001). Primary events in the photoactive yellow protein chromophore in solution. *Chem. Phys. Letters* **336**, 439–444.
39. Larsen, D.S., van Stokkum, I.H.M., Vengris, M., van der Horst, M.A., de Weerd, F.L., Hellingwerf, K.J., van Grondelle, R., (2004). Incoherent manipulation of the photoactive yellow protein photocycle with dispersed pump-dump-probe spectroscopy. *Biophys. J.* **87**, 1858–1872.
40. Zhu, J., Paparelli, L., Hospes, M., Arents, J., Kennis, J.T. M., van Stokkum, I.H.M., Hellingwerf, K.J., Groot, M.L.,

(2013). Photoionization and electron radical recombination dynamics in photoactive yellow protein investigated by ultrafast spectroscopy in the visible and near-infrared spectral region. *J. Phys. Chem. B* **117**, 11042–11048.
41. Slavov, C., Hartmann, H., Wachtveitl, J., (2015). Implementation and evaluation of data analysis strategies for time-resolved optical spectroscopy. *Anal. Chem.* **87**, 2328–2336.
42. Poisot, T., Dorlhiac, G.F., Fare, C., van Thor, J.J., (2017). PyLDM - An open source package for lifetime density analysis of time-resolved spectroscopic data. *PLoS Comput. Biol.* **13**, e1005528.
43. Lórenz-Fonfría, V.A., Kandori, H., (2016). Transformation of time-resolved spectra to lifetime-resolved spectra by maximum entropy inversion of the Laplace transform. *Appl. Spectrosc.* **60**, 407–417.
44. Rumbach, P., Bartels, D.M., Sankaran, R.M., Go, D.B., (2015). The solvation of electrons by an atmospheric-pressure plasma. *Nature Commun.* **6**, 7248.
45. Gallmann, L., Jordan, I., Wörner, H.J., Castiglioni, L., Hengsberger, M., Osterwalder, J., Arrell, C.A., Chergui, M., et al., (2017). Photoemission and photoionization time delays and rates. *Struct. Dyn.* **4**
46. Nakato, Y., Abe, K., Tsubomura, H., (1976). Experimental determination of ionization potentials of tetraphenylporphine and metallotetraphenylporphines. *Chem. Phys. Letters* **39**, 358–360.
47. Runge, C., (1895). Über die numerische Auflösung von Differentialgleichungen. *Math. Ann.* **46**, 167–178.
48. Kutta, W., (1901). Beitrag zur näherungsweisen Integration totaler Differentialgleichungen. Teubner.
49. Kumar, S., Nussinov, R., (1999). Salt bridge stability in monomeric proteins. *J. Mol. Biol.* **293**, 1241–1255.
50. Desiraju, G., Steiner, T., (2001). The Weak Hydrogen Bond. Oxford University Press.
51. Yang, X., Stojković, E.A., Kuk, J., Moffat, K., (2007). Crystal structure of the chromophore binding domain of an unusual bacteriophytochrome, RpBphP3, reveals residues that modulate photoconversion. *Proc. Natl. Acad. Sci.* **104**, 12571–12576.
52. Konold, P.E., van Stokkum, I.H.M., Muzzopappa, F., Wilson, A., Groot, M.-L., Kirilovsky, D., Kennis, J.T.M., (2018). Photoactivation mechanism, timing of protein secondary structure dynamics and carotenoid translocation in the orange carotenoid protein. *J. Am. Chem. Soc.* **141**, 520–530.